Proceedings of the Combustion Institute 40 (2024) 105431

Contents lists available at ScienceDirect

Proceedings of the Combustion Institute

journal homepage: www.elsevier.com/locate/proci

Effect of confinement on the propagation patterns of lean hydrogen–air flames

Anne Dejoan [a], Zhenghong Zhou [b], Daniel Fernández-Galisteo [a,*], Paul D. Ronney [b], Vadim N. Kurdyumov [a]

[a] Department of Energy, Centro de Investigaciones Energéticas, Medioambientales y Tecnológicas, Avda. Complutense 40, 28040, Madrid, Spain
[b] Department of Aerospace and Mechanical Engineering, University of Southern California, Los Angeles, CA, USA

ARTICLE INFO

Keywords:
Hydrogen
Premixed flame
Hele-Shaw cell
Confined flow
Diffusive-thermal instability

ABSTRACT

The effect of confinement on the propagation of lean hydrogen–air flames in a Hele-Shaw cell, formed by two parallel plates separated by a small distance, is studied numerically. The influence of momentum loss on the flame structure and propagation rates is analyzed by examining two limits: (i) the limit of very small distance between the plates, for which a quasi-three-dimensional (quasi-3D) Darcy's law-based approximation is used, and (ii) the limit of unconfined geometry, for which the full set of two-dimensional (2D) Navier-Stokes equations is considered. The influence of heat losses is also included. The chemistry is described by a one-step reduced kinetics with a simple model for transport properties. The results demonstrate that momentum loss primarily increases the flame surface area by elongating the cellular structures in a finger-like form, with a relatively small enhancement of the reactivity at the flame front, consistent with a mechanism of hydrodynamic nature. This elongation leads to approximately a 50% increase in flame speed compared to the absence of confinement. Conversely, heat losses are observed to flatten the large-scale continuous flame front and, if significant enough, can lead to the formation of isolated propagating flame cells of the two-headed or, ultimately, one-headed type. The present results are in good agreement with recent experiments.

1. Introduction

The present work is motivated by recent experimental observations of the propagation patterns of lean hydrogen–air flames in Hele-Shaw cells [1–5]. When the separation distance, d, between the plates of the Hele-Shaw cell is relatively large compared with the thermal thickness of the planar flame, δ_T (with $\delta_T = D_T/S_L$, where S_L is the velocity of the planar adiabatic flame and D_T is the thermal diffusivity of the fresh gas mixture), the experiments show continuous flame fronts characterized by angular sawtooth-shaped structures at the large scales and small cellular structures at the small scales [4–7]. However, as the distance d is significantly reduced, the experiments reveal the existence of isolated flame cells that propagate steadily in the form of a one-headed or two-headed cell type, eventually evolving into fractal or dendrite-like structures [1–5].

In Fig. 1, the impact of d on a flame propagating in a lean H_2-O_2-N_2 mixture (equivalence ratio $\phi = 0.3$) is illustrated. Fig. 1 (top) shows a continuous flame front for $d = 1.27$ cm, where the small scales, evolving into the larger ones, can be identified. Due to the high dilution of this mixture with N_2, the adiabatic temperature, T_{ad}, is only 900 K. This partially explains the small amplitude of the large scales, associated to the Darrieus–Landau instability. The cellular character of the corrugation results from the diffusive-thermal instability. When the gap size is reduced to $d = 0.64$ cm, Fig. 1 (bottom) shows a tendency for the formation of isolated cells.

The phenomenon of the propagation of isolated cells is observed for lean hydrogen–air mixtures and represents an anomaly compared to the traditional quenching limit defined by a Peclet number, $Pe = d/\delta_T$, of order 40 [8]. Actually, experimental investigations using other mixtures such as methane or propane in air [9–14] have consistently failed to yield values of the Peclet number below 50. Consequently, the survival of these isolated cellular structures at Peclet numbers much smaller than the traditional quenching limit requires differential diffusion, with an effective Lewis number sufficiently small. A combustion regime of this nature is of particular relevance, for example, in confined geometries, such as those found in the interstitial spaces between the anode and cathode stacks in a fuel cell [15]. Hydrogen leakage may result in the formation of the isolated flame cell regime during the discharge of any residual voltage, potentially leading to deflagration or explosion in other parts of the device.

The propagation of lean hydrogen–air flames have been extensively investigated in 2D simulations employing detailed chemistry and

* Corresponding author.
E-mail address: d.galisteo@ciemat.es (D. Fernández-Galisteo).

https://doi.org/10.1016/j.proci.2024.105431
Received 4 December 2023; Accepted 13 June 2024

transport [16–21]. These numerical studies confirm the existence of two characteristic length scales (small cellular structures embedded into larger cusp-like patterns), aligned with the experiments [4–7]. Nevertheless, in cases of very small ratios d/δ_T, classical 2D simulations cannot capture the effect of confinement (losses of momentum and heat) inherent to the Hele-Shaw cell when the plates are in very close proximity.

In this work, we address this drawback by employing the quasi-3D approximation, a method previously derived in the limit of small gap distances compared to the flame thickness [22–25]. To provide a comprehensive assessment of the confinement effect, the quasi-3D results are compared with those obtained within the classical 2D Navier–Stokes form, where gas-wall friction effects are absent. The flame patterns are analyzed for cases with adiabatic plates and in the presence of heat losses.

2. Configuration and mathematical formulation

The propagation of a premixed hydrogen–air flame with equivalence ratio $\phi = 0.4$ and initial temperature $T_u = 298$ K is investigated numerically in a Hele-Shaw cell. We consider the case where the flame propagates from an open end (exposed to the atmosphere) to a closed end. With this configuration the flame propagates into a quiescent gas.

2.1. Quasi-3D formulation

In the mathematical limit of $d/\delta_T \to 0$, and with plate wall thickness d_w satisfying $d_w \sim d$, the complete 3D governing equations, see [22], written in a reference frame moving at velocity U, can be reduced to the following 2D set of equations:

$$\frac{\partial \rho}{\partial t} + \nabla \cdot [\rho(\mathbf{u} - U)] = 0, \tag{1}$$

$$\mathbf{u} = -\frac{d^2}{12\mu}\nabla p, \tag{2}$$

$$\frac{\partial}{\partial t}(\rho Y_k) + \nabla \cdot [\rho Y_k(\mathbf{u} - U)] = \frac{1}{Le_k}\nabla \cdot \left(\frac{\lambda}{c_p}\nabla Y_k\right) + \dot{\omega}_k W_k, \tag{3}$$

$$\frac{\partial}{\partial t}(\rho T) + \nabla \cdot [\rho T(\mathbf{u} - U)] = \nabla \cdot \left(\frac{\lambda}{c_p}\nabla T\right) + \frac{\lambda}{c_p^2}\nabla c_p \cdot \nabla T - \frac{1}{c_p}\sum_{k=1}^{N} \mathrm{h}_k^0 \dot{\omega}_k W_k - \frac{1}{c_p}\underbrace{\frac{2\lambda_w}{d\, d_w}}_{b}(T - T_u), \tag{4}$$

with the ideal gas equation of state given by

$$\frac{\rho \mathcal{R} T}{W} = p_{\mathrm{atm}}. \tag{5}$$

In the above formulation, the flow properties are averaged across the gap d, and the momentum equation is reduced to the linear relation (2), similar to Darcy's law. This formulation is referred now and below to as the quasi-3D approximation. Note that, although Eq. (2) shows an apparent dependence on d, this dependence is eliminated when the full set of equations is combined (see Appendix 1). The wall-heat losses are introduced through the heat-loss parameter b in Eq. (4). For laminar flows in plane channels, the Nusselt number based on hydraulic diameter d_H is given by $Nu \equiv h d_H/\lambda \approx 7.4$ [26], with h the convective heat transfer and λ the thermal conductivity of the gas mixture. For channels much wider in the spanwise direction than their height d, as in Hele-Shaw cells, $d_H \approx 2d$ and thus $h \approx 3.7\lambda/d$ and consequently $b \approx 3.7\lambda/d^2$. Since the acrylic or glass plates used in experiments have much higher ρ and λ than gases, it is reasonable to assume that the plate temperatures remain close to T_u and thus the form of heat loss shown in Eq. (4) is an appropriate representation of the cited experiments. For a nominal $d = 1$ mm, with $\lambda \approx 0.026$ W/mK, $b \approx 9.6 \times 10^4$ W/m^{3}K. Consequently, values of b on the order of 1×10^5 W/m^{3}K will be employed in the calculations with heat loss in Section 4.2.

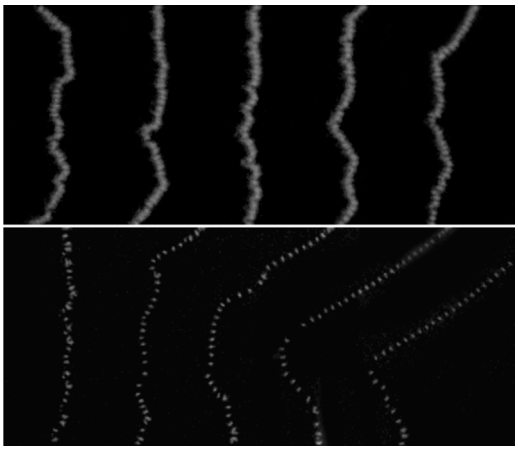

Fig. 1. Sequential, superimposed images of a flame propagating from left to right in a Hele-Shaw cell in a 7.3%H_2 - 12.3%O_2 - 80.4%N_2 mixture ($\phi = 0.3$, $T_{ad} = 900$ K) with a gap size $d = 1.27$ cm (top) and $d = 0.64$ cm (bottom) [27]. Records made with a high-speed intensified video sensitive to near-IR emissions (823 nm), where H_2O has a weak emission band. Field of view is 107 cm × 46 cm.

The variables $\mathbf{u} = (u, v)$, ρ, T, and p stand for the velocity field, density, temperature and hydrodynamic pressure, respectively. Within the low-Mach number approximation employed here, the hydrodynamic pressure variations are much smaller than the thermodynamic pressure ($p_{\mathrm{atm}} = 1$ atm) and therefore p is decoupled from the equation of state (5). Y_k, h_k^0, $\dot{\omega}_k$ and W_k denote the mass fraction, formation enthalpy, reaction rate, and molecular weight of the species k; μ is the dynamic viscosity; Le_k is the Lewis number of the species k; c_p is the heat capacity of the gas mixture; $\mathcal{R}$ is the universal gas constant; and W is the mean molecular weight.

Following [28], species diffusivities are imposed by setting spatially homogeneous Lewis numbers, with $Le_{H_2} = 0.3$, $Le_{O_2} = 1.11$, and $Le_{H_2O} = 0.83$, and the thermal conductivity of the gas is computed with the approximation $\lambda/c_p = 2.58 \times 10^{-5}(T/T_u)^{0.7}$ kg/(m s), with c_p evaluated by NASA polynomials. Soret diffusion is not included, but its overall effects are quantified in Appendix B.

2.2. 2D formulation

In addition to the quasi-3D problem, numerical simulations are also performed with the classical 2D form, where the momentum equation

$$\frac{\partial(\rho \mathbf{u})}{\partial t} + \nabla \cdot [\rho \mathbf{u}(\mathbf{u} - U)] = -\nabla p + \nabla \cdot \mu[(\nabla \mathbf{u} + \nabla \mathbf{u}^{\mathrm{T}}) - 2/3(\nabla \cdot \mathbf{u})\mathbf{I}], \tag{6}$$

is solved, instead of (2). Note that the heat-loss term in Eq. (4) has to be re-interpreted as a volumetric heat loss in the 2D simulations, where walls are absent.

2.3. Chemical kinetics

The chemistry is described by the one-step reduced kinetics developed in [29] for lean hydrogen–air flames, and generalized in [30] for general stoichiometry. It employees only $N = 3$ species (H_2, O_2, and H_2O) instead of the 8 species (H_2, O_2, H_2O, H, O, OH, HO_2, and H_2O_2) involved in the detailed kinetics [31]. Compared to the fully detailed chemistry, the one-step kinetics has the advantage of including the main steps of the chemical reactions tackling the relevant physics at a low computational cost. This kinetics is applicable to mixtures with a burnt temperature close to the crossover temperature, resulting in intermediate species being present in small quantities; see [32].

Table 1 shows key parameters determined using the one-step kinetics with simple transport and the detailed chemistry with detailed transport.

Table 1
Characteristic values of the planar flame velocity, thermal flame thickness, and adiabatic temperature calculated for $\phi = 0.4$, $T_u = 298$ K, and at 1 atm.

Parameter (units)	One-step	Detailed
S_L (cm)	32.8	24.5
δ_T (mm)	0.097	0.131
T_{ad} (K)	1436	1424

2.4. Boundary and initial conditions

Governing equations are integrated within a rectangular domain of dimensions $L_x \times L_y$ with the general boundary conditions

$$\begin{aligned} x = 0: &\quad p = \partial T/\partial x = \partial Y_k/\partial x = 0, \\ x = L_x: &\quad u = T - T_u = Y_k - Y_{k,u} = 0, \end{aligned} \tag{7}$$

in the streamwise x-direction, where $Y_{k,u}$ is the mass fraction of the unburnt species k, and with periodic conditions in the spanwise y-direction.

In the simulations with adiabatic plates, the computations are initialized by introducing a small-amplitude sinusoidal perturbation to the planar, unstretched premixed flame. The wavenumber of the perturbation is chosen to be close to the value that maximizes the growth rate in the linear stability regime, as was done in [19]. The planar flame solution rapidly destabilizes into cups and cells, thereby shortening the transition time to a well-established non-linear regime. To track the flame front, a reference frame moving at velocity U equal to the consumption speed S_c, with $S_c = -\int_0^{L_x}\int_0^{L_y} \dot{\omega}_{H_2}\,\mathrm{d}x\,\mathrm{d}y/(\rho_u Y_{H_2,u} L_y)$, is implemented according to [33], enabling the flame to remain within the computational domain.

In the simulations with heat losses, the long-term solution obtained from the adiabatic case is taken as the initial condition. Heat losses are systematically increased to explore their impact on the propagation pattern until flame extinguishes.

3. Numerical treatment

The numerical code employed for the integration of the governing equations is the Open source Field Operation And Manipulation (OpenFOAM) toolbox [34]. The equations are discretized on a collocated grid arrangement making use of the finite volume method. The PIMPLE algorithm is applied for the pressure–velocity coupling to ensure mass conservation. Temporal discretization is performed through a first-order Euler scheme while a second-order scheme is used for spatial discretization.

The computational domain is large enough to resolve all characteristics flame scales [19]. In particular, $L_x = 700\delta_f$ and $L_y = 375\delta_f$, with $\delta_f = 0.32$ mm the thickness of the planar flame defined by $\delta_f = (T_{ad} - T_u)/\max(\mathrm{d}T/\mathrm{d}n)$. The choice of δ_f for the scaling, instead of δ_T, facilitates direct comparison with previous works [19–21]. For the simulations with heat loss, the spanwise size can be reduced to $L_y = 95\delta_f$ (see justification in Section 4.2). An uniform Cartesian grid is employed, with grid resolution $\Delta_x = \Delta_y = 0.18\delta_f$ for the adiabatic case and up to $0.09\delta_f$ for the case with heat loss.

The time step is fixed to a small value to maintain numerical stability, with a value of $\Delta t = 10^{-3}\tau_f$, where $\tau_f = \delta_f/S_L \approx 10^{-3}$ s is the characteristic time associated to the laminar flame. The total physical time simulated is $t \approx 0.35$ s ($350\tau_f$).

4. Results and discussion

4.1. Adiabatic simulations

The impact of momentum loss is depicted in Fig. 2, where the time evolution of the overall propagation rate S_c/S_L is compared using both

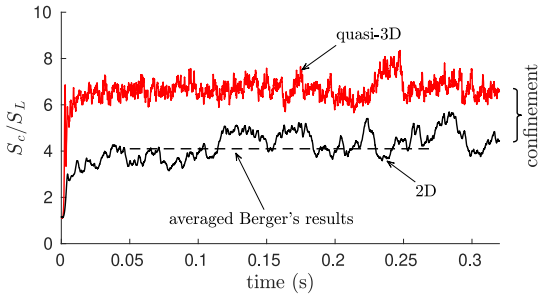

Fig. 2. Time evolution of the propagation rate S_c/S_L for the quasi-3D and the 2D simulations. The dashed line represents the average value reported by Berger et al. [19,20].

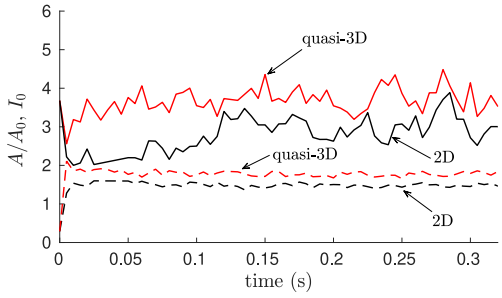

Fig. 3. Time evolution of the flame surface area A/A_0 (solid curves) and the stretch factor I_0 (dashed curves) for the quasi-3D and the 2D simulations.

the quasi-3D and the 2D formulation. Momentum loss enhances the propagation velocity by about 50% with respect to the case with no gas-wall friction. Fig. 2 also shows in dashed line the average propagation rate obtained previously by Berger et al. [19,20] in 2D simulations. These authors report a value of $\langle S_c\rangle/S_L \approx 4.1$ while our 2D simulations yield $\langle S_c\rangle/S_L \approx 4.4$.

To better clarify the factors contributing to the increment of the propagation velocity, the overall propagation rate is decomposed in two terms, as done in [19–21], namely,

$$\frac{S_c}{S_L} = \frac{A}{A_0} I_0, \tag{8}$$

where A is the total flame surface area, A_0 is the reference surface area of planar flame ($A_o = L_y$), and I_0 is the stretch factor, representative of deviation from unstretched flame due to local reactivity and flame front structure. Eq. (8) shows that the propagation rate increases from wrinkling (A/A_0) or from local burning associated to differential diffusion (I_0). The area A is given by $A = \int \delta(C_{H_2} - C_0)|\nabla C_{H_2}|\,\mathrm{d}x\,\mathrm{d}y$, where C_{H_2} is a progress variable defined by $C_{H_2} = 1 - Y_{H_2}/Y_{H_2,u}$, and C_0 is a selected reactive iso-surface, fixed to 0.9, as done in [20].

Fig. 3 compares the time evolution of A/A_0 and I_0 between the quasi-3D and 2D simulations. Notably, momentum loss does not significantly increase I_0, which is around $I_0 \approx 2$ in both cases and close to $I_0 = 2.1$ reported in [20]. Instead, loss of momentum primarily enhances the surface area (A/A_o), highlighting the hydrodynamic character of the momentum loss effect.

In Fig. 4, instantaneous quasi-3D and 2D flame fronts are illustrated using the relative power emissivity field of water, defined as the power emissivity of water normalized by the maximum emission in the planar flame. The power emissivity is calculated multiplying the water mole fraction by the Planck function at wavelength 823 nm and the actual temperature. This facilitates a visual comparison with the experiments shown in Fig. 1. Under loss of momentum, the corrugated flame front exhibits more elongated cells, resembling a finger-like form penetrating into the fresh mixture. This elongation is responsible of the increase of A/A_o displayed in Fig. 3. Not shown, temperature maxima of 1760 K

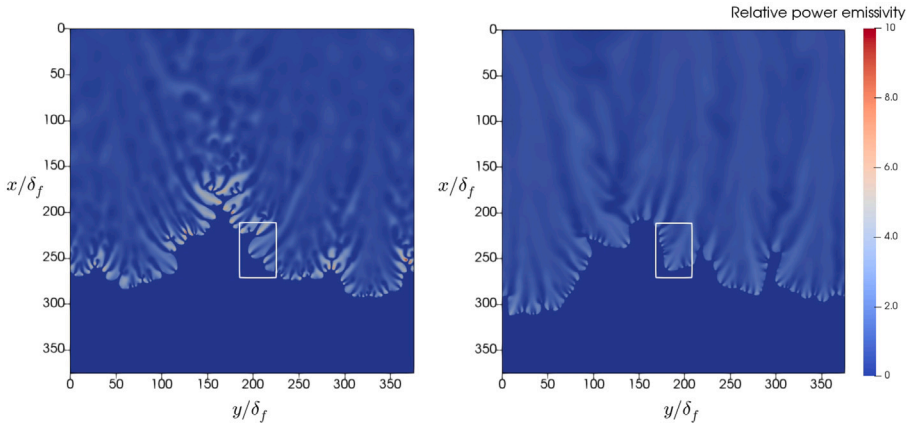

Fig. 4. Relative power emissivity field of water at time $t = 0.3$ s ($\sim 300\delta_f/S_L$) for the quasi-3D simulation (left) and the 2D simulation (right). The white box ($60\delta_f \times 40\delta_f$) is drawn to highlight the characteristic flame scales, as done in [19].

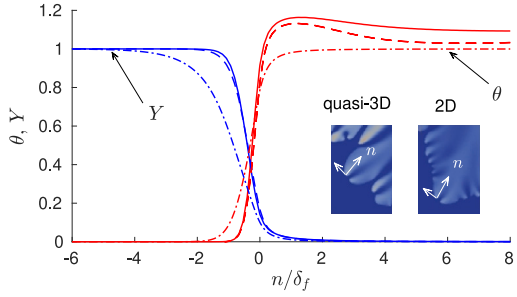

Fig. 5. Profiles of the normalized temperature $\theta = (T - T_u)/(T_{ad} - T_u)$ and H_2 mass fraction, $Y = Y_{H_2}/Y_{H_2,u}$, along a streamwise section n, as marked in the corresponding insets. Solid curves: quasi-3D case; dashed curves: 2D case; dot-dashed curves: planar flame solution.

are observed in some convex part of the cells in the quasi-3D case, surpassing those in the 2D case (1610 K). This temperature increase is associated with the rise of I_0 compared to the 2D case (see Fig. 3). It is worth to mention that the flame structure drawn in Fig. 4 (right) is in satisfactory agreement with the simulations results in [19–21], even though the authors employed a detailed chemistry. In particular, the area marked with a rectangular white box for the 2D case shows the same flame scales as in [19].

Fig. 5 depicts the profiles of the normalized temperature, θ, and hydrogen mass fraction, Y, along a streamwise section across the most convex part of the advanced flame front noses. The quasi-3D and 2D profiles are compared with that of the planar unstretched flame. As expected for a thermo-diffusive flame with a small Lewis number, the flux of H_2 is increased to the curved flame front, which increases the burning rate and the temperature of the products. However, Fig. 5 does not show an appreciable difference between the quasi-3D and 2D simulations. This reinforces the idea of the essential hydrodynamic mechanism of the momentum loss, as examined earlier in Fig. 3.

4.2. Simulations with heat loss

In the presence of heat losses, the large scales of the flame front observed in Fig. 4 tends to flatten, while the small cellular scales persist. This behavior is illustrated in Fig. 6 for $b = 2 \times 10^5$ W/m^{3}K. Note that the power emissivity is maximal at the small crests of the front, and becomes even more intense in the presence of confinement, reflecting higher local reactivity.

The decrease in amplitude observed for the large scales in Fig. 6 suggests that a reduced size of L_y can be employed in the simulations, consequently allowing an increase of the numerical resolution. In what follows, heat losses are examined within a truncated domain with $L_y = 95\delta_f$, and with a higher grid resolution of $0.09\delta_f$, in comparison to the larger computational domain considered thus far.

Fig. 7 depicts the temporal evolution of S_c/S_L for different values of the heat-loss parameter b. As expected, increasing b reduces the overall propagation rate until flame extinction occurs. The impact of the momentum loss appears to be important even in cases with large heat losses. Note, for example, that the propagation rate in the quasi-3D simulation is nearly twice that of the 2D case for $b = 2 \times 10^5$ W/m^{3}K. Above a critical value of $b \approx 2.9 \times 10^5$ W/m^{3}K, Fig. 7 shows curves with a steady evolution of S_c/S_L, which represents the emergence of isolated flame cells (see below). In these latter cases, S_c does not longer characterize the real flame velocity and, instead, the displacement velocity of the flame cells must be considered.

The normalized displacement velocity, S_d/S_L, calculated by evaluating the distance covered by the flame front between two consecutive times, is depicted in Fig. 8 as a function of b. The propagation velocities of the corresponding isolated cells are marked with empty circles. In addition, Fig. 8 displays the average propagation velocity $\langle S_c \rangle/S_L$ of the cases with continuous flame front, marked with solid circles. The propagation velocities of the quasi-3D simulations are shown to be well above those of the 2D cases and so, extinction occurs for high values of b in the quasi-3D simulations. The critical $b \approx 2.9 \times 10^5$ W/m^{3}K delimits the boundary between the two distinct regimes of flame propagation.

The structure of the steady-propagating cells is illustrated in Fig. 9 for $b = 2.9 \times 10^5$ W/m^{3}K by considering the water mass fraction field. This latter provides a reliable marker for tracing back the path of the flame evolution. Figs. 9(a)-(b) exhibit a two-headed pattern, with local reactivity (not shown) only at the head of the cells. While the characteristic width of the cells (indicated by white arrows) is close in both quasi-3D and 2D cases (around $11.7\delta_f$), the quasi-3D simulation displays a more elongated form, leading to the increase of velocity observed in Fig. 8.

Only shown for the quasi-3D simulations, but similarly observed in the 2D cases, Figs. 10(a)-(b) illustrate the decrease in cell width with heat loss. It is interesting to note that close to extinction, the two-headed cells separate and evolve into two one-headed cells, see Fig. 10(c). The one-headed cells obtained extinguish shortly after their formation and do not exhibit steady propagation, in contrast to the findings reported in [3,24]. The dynamics of the one-headed cells observed in this study calls for further numerical investigation, as the small size of these cells may require a higher grid resolution for accurate analysis.

The steady character of the two-headed cells aligns with the experimental findings in [1–3], as well as with the recent numerical study presented in [24]. The size of the two-headed cells explored here (ranging from $7.8\delta_f$ to $11.8\delta_f$) are consistent with the values (ranging

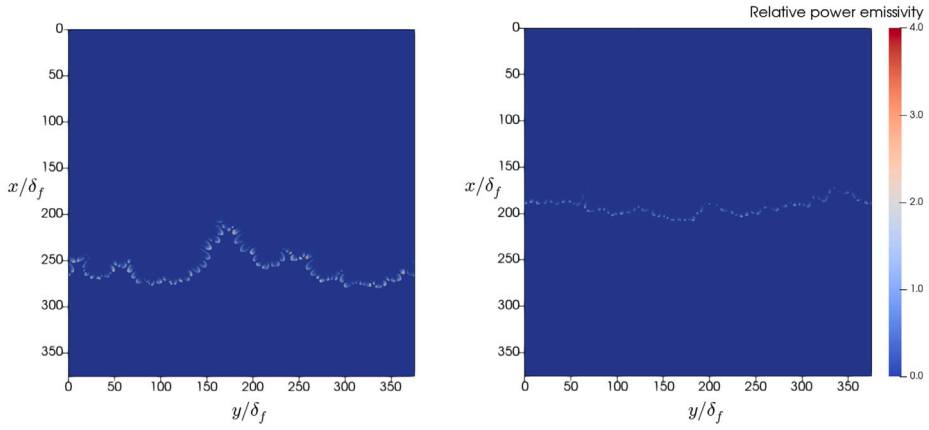

Fig. 6. Relative power emissivity field of water at time $t = 0.15$ s ($\sim 150\delta_f/S_L$) for the quasi-3D simulation (left) and the 2D simulation (right) with $b = 2 \cdot 10^5$ W/(m^3 K).

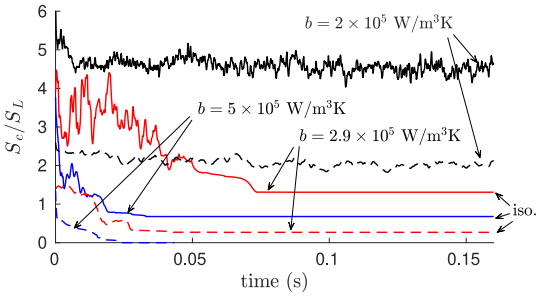

Fig. 7. Time evolution of the propagation rate S_c/S_L for the quasi-3D (solid curves) and the 2D (dashed curves) cases with different values of the heat-loss parameter.

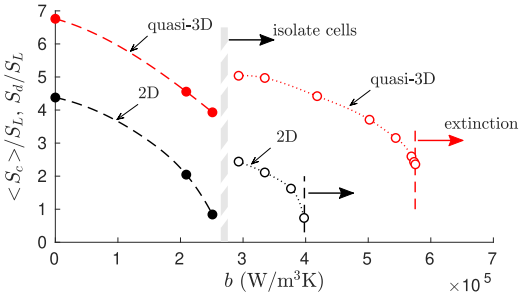

Fig. 8. Displacement velocity S_d/S_L of the isolated flame cells with b for the quasi-3D (solid circles) and the 2D (empty circles) cases. Vertical dashed lines to the right mark flame extinction.

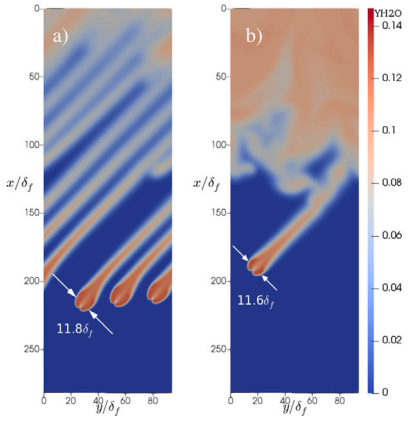

Fig. 9. Visualization of the water mass fraction field given for $b = 2.9 \times 10^5$ W/m^{3}K for (a) quasi-3D and (b) 2D. White arrows indicate flame finger size.

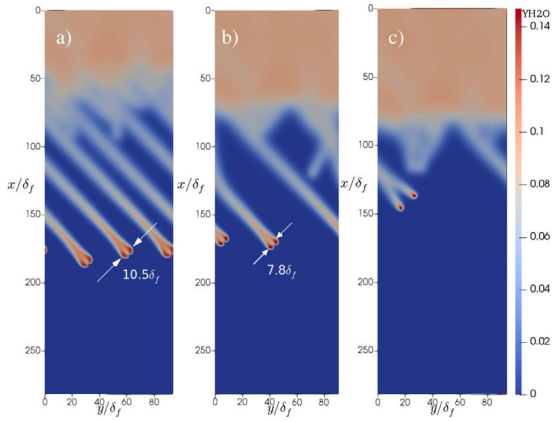

Fig. 10. Visualization of the water mass fraction field given for quasi-3D simulations with (a) $b = 5 \cdot 10^5$ W/(m^3 K), (b) $b = 5.7 \cdot 10^5$ W/(m^3 K), and (c) $b = 5.8 \cdot 10^5$ W/(m^3 K). White arrows indicate flame finger size. Case (c) is an instantaneous view of a one-headed cell before extinction.

from $5\delta_f$ to $9\delta_f$) reported for the characteristic cellular size in 2D adiabatic simulations in [21]. This agreement suggests the robustness of the cellular structure to heat losses.

Notably, lateral motion has been observed experimentally [6] and numerically [19,20] in previous 2D studies, but further investigation is required to explain this phenomenon in the case of isolated cells.

5. Conclusions

This study presents numerical simulations of lean premixed hydrogen–air flames propagating in a Hele-Shaw cell. The effect of momentum and heat loss, inherent to this geometry, is analyzed by employing a quasi-3D formulation based on Darcy's law. The chemistry is described by a one-step reduced kinetics, which reproduces the essential characteristics of hydrogen deflagrations. The influence of momentum loss is examined by comparing results obtained from the quasi-3D formulation with those from an unconfined 2D formulation. The results show that momentum loss increases the flame surface area and, consequently, the overall propagation rates due to further elongation of the cellular structures. In the presence of heat losses, isolated two-headed flame cells appear (one-headed cells were found to extinguish). The effect of momentum loss persists even in the presence of heat losses, making the flame cells more robust against extinction.

Novelty and significance statement

The novelty of this research is the analysis of both the momentum and heat loss effects on the propagation of a lean hydrogen-air flame through a confined geometry, specifically a Hele-Shaw cell. Most numerical studies in the literature have been performed in unconfined (2D) geometry. However, the analysis of confinement effects is particularly relevant for safety concerns, given the unexpected cellular propagation regimens observed recently in highly confined Hele-Shaw cells for ultra-lean hydrogen-air mixtures [1–4].

CRediT authorship contribution statement

Anne Dejoan: Design, Programmation, Performance of simulations, Analysis of numerical results, Writing. **Zhenghong Zhou:** Performance of experimental part, Discussion of numerical results. **Daniel Fernández-Galisteo:** Design of simulations, Analysis of numerical results, Writing. **Paul D. Ronney:** Design of experimental part, Discussion of numerical results, Analysis of results, Writing. **Vadim N. Kurdyumov:** Design of mathematical approach, Analysis of results, Writing.

Declaration of competing interest

The authors declare that they have no known competing financial interests or personal relationships that could have appeared to influence the work reported in this paper.

Acknowledgments

This study was funding from MICIU/AEI/10.130 39/501100011033, FEDER, and from European Union "NextGenerationEU"/PRTR and PRTR-C17.I1 through projects #PID2022-139082NB-C52 and #TED2021-129446-C42. The USC work was partially supported by the US Department of Energy (ARPA-E) under contract DE-AR0001538. DFG gratefully acknowledges financial support from the Spanish Ministry of Universities through the Mobility Program 2021–2023 (Grant No. PRX22/00715). DFG also acknowledges helpful discussions with Prof. F. A. Williams.

Appendix A

The dependence on d shown in Eq. (2) is discussed here. Taking the divergence of Eq. (2) leads to the following Poisson equation for the pressure

$$\nabla^2 p = \frac{1}{\mu}(\nabla p \cdot \nabla \mu) - \frac{12\mu}{d^2}(\nabla \cdot \mathbf{u}), \tag{9}$$

where the velocity divergence

$$\nabla \cdot \mathbf{u} = \frac{\mathcal{R}}{p_{\text{atm}} W}\left[\nabla \cdot \left(\frac{\lambda}{c_p}\nabla T\right) + \frac{\lambda}{c_p^2}\nabla c_p \cdot \nabla T - \frac{1}{c_p}\sum_{k=1}^{N} \mathrm{h}_k^0 \dot{\omega}_k - \frac{b}{c_p}(T - T_u)\right] + \frac{W}{\rho}\sum_{k=1}^{N}\frac{1}{W_k}\left[\frac{1}{Le_k}\nabla \cdot \left(\frac{\lambda}{c_p}\nabla Y_k\right) + \dot{\omega}_k\right]. \tag{10}$$

is obtained by combining Eqs. (1) and (4), and making use of (5). By simple inspection of (9) and (10), it can be easily verified that the parameter d does not enter in the formulation.

Appendix B

Additional adiabatic simulations with Soret diffusion (not shown) were conducted by introducing the modified H_2 diffusion term $\nabla Y_{H_2} + \alpha_{H_2} Y_{H_2} \nabla T/T$ in Eq. (3), where $\alpha_{H_2} = -0.29$ is the thermal diffusion factor; see [35]. The inclusion of Soret diffusion does not qualitatively alter the effect of confinement on the flame structure observed without Soret diffusion. However, it increases the reactivity in the convex part of the cells, leading to an overall increase in propagation rates by approximately 10%, with $\langle S_c \rangle / S_L \approx 4.8$ for the 2D simulation and $\langle S_c \rangle / S_L \approx 7.5$ for the quasi-3D simulation.

References

[1] F. Veiga-López, M. Kuznetsov, D. Martínez-Ruiz, E. Fernández-Tarrazo, J. Grune, M. Sánchez-Sanz, Unexpected propagation of ultra-lean hydrogen flames in narrow gaps, Phys. Rev. Lett. 124 (2020) 174501.
[2] J. Yáñez, M. Kuznetsov, F. Veiga-López, Characterization of unconventional hydrogen flame propagation in narrow gaps, Phys. Rev. E 103 (2021) 033101.
[3] R. Palomeque-Santiago, A. Domínguez-González, M. Rubio-Rubio, E. Fernández-Tarrazo, D. Martínez-Ruiz, M. Sánchez-Sanz, Experimental evidence of the multiplicity of stationary solutions in ultra-lean hydrogen flames, in: Proceedings of the 11th European Combustion Meeting, 2023, pp. 228–230.
[4] P.V. Moskalev, V.P. Denisenko, I.A. Kirillov, Classification and dynamics of ultralean hydrogen-air flames in horizontal cylindrical Hele-Shaw cells, J. Exp. Theor. Phys. 137 (2023) 104–113.
[5] Z. Zhou, S. Shen, J. Weiss, P.D. Ronney, Characteristics of H2-o2-N2 flames in quasi-2D channels: Propagation rates and scaling parameters, in: 13th U.S. National Combustion Meeting, College Station, TX, March 20 - 22, 2023.
[6] F. Veiga-López, D. Martínez-Ruiz, M. Kuznetsov, M. Sánchez-Sanz, Thermoacoustic analysis of lean premixed hydrogen flames in narrow vertical channels, Fuel 278 (2020) 118212.
[7] G. Gu, J. Huang, W. Han, C. Wang, Propagation of hydrogen-oxygen flames in Hele-Shaw cells, Int. J. Hydrog. Energy 56 (2021) 12009–12015.
[8] J. Jarosinski, Flame quenching by a cold wall, Combust. Flame 50 (1983) 167–175.
[9] J. Sharif, M. Abid, P.D. Ronney, Premixed-Gas Flame Propagation in Hele-Shaw Cells, Tech. rep., Spring Technical Meeting, joint U.S. Sections, Combustion Institute, 1999, pp. 352–355.
[10] C. Almarcha, J. Quinard, B. Denet, E. Al-Sharraf, J.M. Laugier, E. Villermaux, Experimental two dimensional cellular flames, Phys. Fluids 27 (2015) 91110.
[11] E. Al-Sarraf, C. Almarcha, J. Quinard, B. Radisson, B. Denet, P. García-Ybarra, Darrieus-Landau instability and Martkstein numbers of premixed flames in a Hele-Shaw cell, Proc. Combust. Inst. 37 (2019) 1783–1789.
[12] F. Veiga-López, D. Martínez-Ruiz, E. Fernández-Tarrazo, M. Sánchez-Sanz, Experimental analysis of oscillatory premixed flames in a Hele-Shaw cell propagating towars a closed end, Combust. Flame 201 (2019) 1–11.
[13] D. Martínez-Ruiz, F. Veiga-López, M. Sánchez-Sanz, Premixed-flame oscillations in narrow channels, Phys. Rev. Fluids 4 (2019) 100503.
[14] M.M. Alexeev, O.Y. Semenov, S.E. Yakush, Experimental study on cellular premixed propane flames in a narrow gap between parallel plates, Combust. Sci. Technol. 191 (2019) 1256–1275.
[15] M. Kuznetsov, J. Grune, Experiments on combustion regimes for hydrogen/air mixtures in a thin layer geometry, Int. J. Hydrog. Energy 44 (2019) 8727–8742.
[16] C. Atlantis, C.E. Frouzakis, A.G. Tomboulides, S.G. Kerkemeir, K. Boulouchos, Detailed numerical simulations of intrinsically unstable two-dimensional planar lean premixed hydrogen/air flames, Proc. Combust. Inst. 33 (2011) 1261–1268.
[17] C. Altantzis, C.E. Frouzakis, A.G. Tomboulides, M. Matalon, Hydrodynamic and thermodiffusive instability effects on the evolution of laminar planar lean premixed hydrogen flames, J. Fluid Mech. 700 (2012) 329–361.
[18] C.E. Frouzakis, N. Fogla, A.G. Tomboulides, C. Altantzis, M. Matalon, Numerical study of unstable hydrogen/air flames: Shape and propagation speed, Proc. Combust. Inst. 35 (2015) 1087–1095.
[19] L. Berger, K. Kleinheinz, A. Attili, H. Pitsch, Characteristic patterns of thermodiffusively unstable premixed lean hydrogen flames, Proc. Combust. Inst. 37 (2019) 1879–1886.
[20] L. Berger, M. Grinberg, B. Jürgens, P.E. Lapenna, F. Creta, A. Attili, H. Pitsch, Flame fingers and interactions of hydrodynamic and thermodiffusive instabilities in laminar lean hydrogen flames, Proc. Combust. Inst. 39 (2023) 1525–1534.
[21] L. Berger, A. Attili, H. Pitsch, Intrinsic instabilities in premixed hydrogen flames: Parametric variation of pressure, equivalence ration, and temperature. Part 2 - non-linear regime and flame speed enhancement, Combust. Flame 240 (2023) 111936.
[22] D. Fernández-Galisteo, V.N. Kurdyumov, P.D. Ronney, Analysis of premixed flame propagation between two closely-spaced parallel plates, Combust. Flame 190 (2018) 133–145.
[23] D. Martínez-Ruiz, F. Veiga-López, D. Fernández-Galisteo, V.N. Kurdyumov, M. Sánchez-Sanz, The role of conductive heat losses on the formation of isolated flame cells in Hele-Shaw chambers, Combust. Flame 209 (2019) 187–199.
[24] A. Domínguez-González, D. Martínez-Ruiz, M. Sánchez-Sanz, Stable circular and double-cell lean hydrogen-air premixed flames in quasi two-dimensional channels, Combust. Flame 241 (2023) 112109.
[25] D. Fernández-Galisteo, A. Dejoan, J. Melguizo-Gavilanes, V.N. Kurdyumov, A three-dimensional study of the influence of momentum loss on hydrodynamically unstable premixed flames, Proc. Combust. Inst. 39 (2023) 1545–1554.
[26] R.K. Shah, A.L. London, Laminar Flow: Forced Convection in Ducts, Academic Press, 1978.
[27] Z. Zhou, Propagation Rates, Instabilities, and Scaling for Hydrogen Flames (Ph.D. thesis), University of Southern California, 2023.
[28] M.D. Smooke, V. Giovangigli, Formulation of the premixed and non-premixed test problems, in: M.D. Smooke (Ed.), Reduced Kinetic Mechanisms and Asymptotic Approximations for Methane-Air Flames, in: Lecture Notes in Physics, vol. 384, Springer-Verlag, Heidelberg, 1991, pp. 1–28.

[29] D. Fernández-Galisteo, A.L. Sánchez, A. Liñán, F.A. Williams, One-step reduced kinetics for lean hydrogen-air deflagration, Combust. Flame 156 (2009) 985–996.
[30] D. Fernández-Galisteo, A. Weiss, A.L. Sánchez, F.A. Williams, A one-step reduced mechanism for near-limit hydrogen combustion with general stoichiometry, Combust. Flame 208 (2019) 1–4.
[31] Chemical-kinetic mechanisms for combustion applications, in: San Diego Mechanism web page, Mechanical and Aerospace Engineering (Combustion Research), University of California at San Diego, Version 16-12-14, http://web.eng.ucsd.edu/mae/groups/combustion/mechanism.html.
[32] D. Fernández-Galisteo, A.L. Sánchez, A. Liñán, F.A. Williams, The hydrogen-air burning rate near the lean flammability limit, Combust. Theory Model. 13 (4) (2009) 741–761.
[33] J. Bell, M.S. Day, J.F. Grcar, M.J. Lijewski, Active control for statistically stationary turbulent premixed flame simulations, Commun. Appl. Math. Comput. Sci. 1 (2006) 29–49.
[34] https://www.openfoam.com/.
[35] A.L. Sánchez, F.A. Williams, Recent advances in understanding of flammability characteristics of hydrogen, Prog. Energy Combust. Sci. 41 (2014) 1–55.